FOURTH AUSTRALASIAN CONFERENCE

on

HYDRAULICS AND FLUID MECHANICS

at

Monash University, Melbourne, Australia

1971 November 29 to December 3

BOUNDARY LAYER EFFECTS IN SUPERSONIC FLOW OVER CYLINDER-FLARE BODIES

by

M.L. Robinson*

SUMMARY

The effects of shock wave-boundary layer interaction on the forces acting on cylinder-flare bodies have been investigated experimentally at a Mach number of 2·8. Detailed pressure measurements have been made on axisymmetric models with 15° semi-angle flare afterbodies in the incidence range 0° to 10°. The Reynolds numbers of the tests based on the distance from the nose to the cylinder-flare junction varied between $0{\cdot}8 \times 10^6$ and $2{\cdot}9 \times 10^6$. Force distributions, and total forces and moments were obtained by integration of the measured pressure distributions. The experimental results are compared with the results of inviscid theory to gain an appreciation of the magnitude of shock wave-boundary layer interaction effects. The comparisons have indicated that, in the absence of separation, experiment and inviscid theory agree reasonably well. Where a moderate degree of flow separation occurred, flare lift was significantly increased, and a useful increase in static stability was obtained near zero incidence.

* Senior Research Scientist,
Weapons Research Establishment,
Salisbury, S.A.

1. LIST OF SYMBOLS

B	quantity defined by eqn. (2)
C_A	axial force coefficient, axial force/$q_\infty S_o$
C_N	normal force coefficient, normal force/$q_\infty S_o$
C_m	pitching moment coefficient, pitching moment/$q_\infty S_o L$
C_p	pressure coefficient, $(2/\gamma M_\infty^2)(p/p_\infty - 1)$
D	diameter of cylindrical portion (stem) of model
D_b	base diameter of flare
L	distance from nose to cylinder-flare junction
M	Mach number
R_L	Reynolds number based on length L
S	arbitrary reference area
S_o	reference area, $\pi D^2/4$
U	velocity outside boundary layer
p	static pressure
p_t	total pressure
q	dynamic pressure
r	model radius
u	velocity in boundary layer
x	axial coordinate, measured from nose
x_1, x_2	limits of integration in eqs. (5), (12), (13) and (14)
y	distance from wall
α	incidence
γ	ratio of specific heats, 1·4 for air
δ	flare semi-angle
δ_1	boundary layer thickness
η	quantity defined by eqn. (4)
Λ	loading function defined by eqn. (6)
μ	Mach angle, $\sin^{-1}(1/M)$
σ	shock wave angle
φ	meridian (roll) angle

Subscripts

a_1, a_2 / b, b_1	conditions at various points in flow field, figure 1
cb	conditions on cone at discontinuity "b"
∞	free-stream conditions

2. INTRODUCTION

Flared afterbodies provide a simple means of producing stability of flight vehicles at high Mach numbers without markedly increasing the weight of the vehicle. An additional advantage is that flares provide a natural fairing between various stages of launch configurations. Although flares have been used extensively to stabilize bodies in flight, adequate predictions of the aerodynamic properties of such bodies are not routinely successful. Prediction is not an easy task because of the sensitivity of the flare configuration to the variables involved, namely body geometry, flow parameters and state of the boundary layer. Because of the complexity of the flare-stabilization problem, experimental data is required to define the importance of each factor and to establish the applicability of theoretical methods.

This paper presents results of an experimental and theoretical study of the flow at a Mach number of 2·8 over two cylinder-flare models 0·16 in (4 mm) and 4·00 in (102 mm) diameter. The length of each model from the nose to the cylinder-flare junction was 10·0 in (254 mm), and the semi-angle of the flare on each model was 15·0°. The tests were carried out in the incidence range 0° to 10° in the supersonic wind tunnel at the Aerospace Division of W.R.E. The Reynolds numbers of the tests varied between $0{\cdot}8 \times 10^6$ and $2{\cdot}9 \times 10^6$ based on the 10 in stem length and free-stream conditions. The test programme comprised detailed surface pressure measurements, velocity profile determinations and flow observations using the schlieren method. The surface pressure distributions, which were measured using an automatic pressure scanning system, have provided information on separation characteristics as well as loading distributions and overall forces and moments.

Theoretical pressure distributions, loading distributions and total forces and moments acting on the axisymmetric models have been computed for inviscid flow according to the second-order shock-expansion method of Syvertson and Dennis (1). A particular advantage of this method is that it yields, by its formulation, the correct cone pressure far downstream. The use of the method of linearised characteristics was not considered to be practicable in this application, because of the complexity and the large amount of computing time involved. Reference 1 includes comparisons between computed and experimental results in the Mach number range from 3 to 6, and satisfactory agreement between theory and experiment is demonstrated. Horton (2) presents further comparisons which show that the method maintains its accuracy at Mach numbers as low as 1·32.

3. THEORETICAL ANALYSIS

The Syvertson and Dennis (1) method has been applied to the present problem by considering the flow over a cone-cylinder-flare configuration shown in figure 1. At the discontinuities in slope at "a" and "b", discontinuities in Mach number occur as in the two-dimensional case, but down-stream of each discontinuity the Mach number changes due to convergence effects, instead of being constant as in two-dimensional flow. At the convex discontinuity at "a", the flow is considered isentropic and locally two-dimensional, so that the Prandtl-Meyer relationships are applicable. At the concave discontinuity at "b", allowance is made for the non-isentropic nature of the flow through the shock wave. The pressure variation over the length of the

cylinder and flare, which results from the axisymmetric nature of the flow, is calculated from an exponential curve fitted to the pressure gradient immediately behind the discontinuity, and to the pressure which would exist on a cone of the same semi-vertex angle as the local cone-frustum..

3.1 Pressure Distribution

To simplify the analysis, it will be assumed that the discontinuity "b" in figure 1 is sufficiently remote from "a" such that the pressure gradient $\partial p_{a_2}/\partial x = 0$. The pressure gradient behind the discontinuity at "b" is then given by Syvertson and Dennis to be, in the present notation:

$$\left(\frac{\partial p}{\partial x}\right)_{b_1} = -\left[\frac{1}{1 + \tan \mu_{b_1}/\tan (\sigma_b - \delta_b)}\right] \frac{2B_{b_1}}{r} \sin \delta_b \ , \tag{1}$$

$$\text{where} \quad B_{b_1} = \gamma\, p_{b_1}\, M_{b_1}^2/2\, (M_{b_1}^2 - 1) \ , \tag{2}$$

and p_{b_1} and M_{b_1} are the pressure and Mach number downstream of a two-dimensional shock wave at "b". Since $\partial p_{a_2}/\partial x = 0$, the approach Mach number $M_{a_2} = M_\infty$. The pressure variation along the cone-frustum "bc" is then given by the approximate expression:

$$p = p_{cb} - (p_{cb} - p_{b_1}) \exp(-\eta) \ , \tag{3}$$

$$\text{where} \quad \eta = \left(\frac{\partial p}{\partial x}\right)_{b_1} \frac{x - x_b}{(p_{cb} - p_{b_1}) \cos \delta_b} \ . \tag{4}$$

In equations (3) and (4), p_{cb} is the pressure at a free-stream Mach number M_∞ on a cone of semi-vertex angle δ_b. The cone pressure p_{cb} is obtained from reference (3), and the pressure p_{b_1} downstream of a two-dimensional shock wave is obtained from reference (4).

3.2 Loading Distribution

Attention is restricted to bodies near zero incidence, where it can be demonstrated that the deviation of the true streamlines from the meridian lines will not influence the surface pressures. The expression for the normal force derivative can be written:

$$\frac{dC_N}{d\alpha} = \frac{2\pi}{S_o} \int_{x_1}^{x_2} \Lambda r \, dx \ , \tag{5}$$

where $\frac{dC_N}{d\alpha}$ denotes the zero incidence normal force derivative, Λ is the non-dimensional loading on a disc normal to the body axis and having unit radius, and S_o is a reference area. This loading Λ is given by the equation:

$$\Lambda = \frac{2}{\gamma M_\infty^2 \pi} \int_o^\pi \frac{d(p/p_\infty)}{d\alpha} \cos \varphi \, d\varphi \ . \tag{6}$$

Following the Syvertson and Dennis analysis, equation (6) becomes,

$$\Lambda = \frac{2}{\gamma M_\infty^2 \pi} \int_o^\pi [1 - \exp(-\eta)] \frac{d(p_{cb}/p_\infty)}{d\alpha} \cos \varphi \, d\varphi \ . \tag{7}$$

Equation (7) may be evaluated in terms of the normal force derivative of the tangent cone giving,

$$\Lambda = [1 - \exp(-\eta)] \tan \delta_b \left(\frac{dC_N}{d\alpha}\right)_{cb} \ . \tag{8}$$

Equation (8) has been derived on the basis of isentropic flow at the discontinuity "b" in figure 1, and on the assumption that the total pressure p_t on the flare is independent of φ. It can be shown that equation (8) applies equally well to the flow over a cylinder-flare for which the above conditions are not met provided that, as assumed initially, the pressure gradient $\partial p_{a_2}/\partial x$ is zero. To evaluate the loading using equation (8), the normal force derivative of the tangent cone $\left(\frac{dC_N}{d\alpha}\right)_{cb}$ is obtained from results given in reference 3. When the loading Λ is known, the normal force derivative may be evaluated by integration of equation (5).

4. EXPERIMENTAL DETAILS

The models used in the study are shown in figure 2. The 4·0 in diameter model was a hollow cylinder designed such that the internal flow through the duct did not interfere with the external flow. Because it was not possible to obtain a naturally turbulent boundary layer on this model upstream of the cylinder-flare junction, tests were made with a roughness band consisting of 0·016 in (0·4 mm) glass spheres situated 1·1 in (27·9 mm) from the leading edge. Results obtained with the roughness band are designated by a "t" following the Reynolds number, e.g., $R_L = 2{\cdot}0 \times 10^6 t$. Surface pressures on the models were measured by means of a pressure scanning and recording system incorporating a 15 psia transducer. A limited number of boundary layer surveys were made on the 0·16 in diameter model using a pitot probe whose tip diameter was approximately 10 per cent of the maximum boundary layer thickness. A quantitative schlieren optical system was used to determine the characteristics of the boundary layer on the 4·0 in diameter model. The method involves the analysis of photographic negatives using a microdensitometer, from which density and hence velocity profiles can be obtained. Boundary layer surveys were made on each model at zero incidence only.

5. ANALYSIS OF RESULTS AND UNCERTAINTY OF DATA

Pressure data are presented in the non-dimensional form p/p_∞, where p_∞ is the mean static pressure measured at zero incidence on the model upstream of the interaction region. The estimated error in p/p_∞ for the majority of data presented is ±0·03, and the corresponding error in the pressure coefficient C_p is ±0·005. The normal force distribution on the model is given by,

$$\frac{d(SC_N)}{dx} = 2r\int_0^{\pi} C_p \cos\varphi \, d\varphi \, , \tag{9}$$

and the axial force distribution on the flare by,

$$\frac{d(SC_A)}{dx} = 2r\tan\delta_b \int_0^{\pi} C_p \, d\varphi \, . \tag{10}$$

The quantity $\frac{d(SC_N)}{dx}$ is related to the loading function Λ of Syvertson and Dennis as follows:

$$\frac{d(SC_N)}{dx} = \Lambda\,(2\pi r\alpha) \, , \tag{11}$$

where α is the incidence appropriate to the value of $\frac{d(SC_N)}{dx}$. The integrations in equations (9) and (10) were computed numerically using Simpson's Rule applied to pressure data obtained at roll angles at 30° intervals in the range 0° to 180°.

The total normal force acting on the model is given by integration of the normal force distribution as follows:

$$C_N = \frac{1}{S_o}\int_{x_1}^{x_2}\left[\frac{d(SC_N)}{dx}\right] dx \, . \tag{12}$$

The total pitching moment is given by,

$$C_m = -\frac{1}{S_o}\int_{x_1}^{x_2}\left[\frac{d(SC_N)}{dx}\right]\left[\frac{x-L}{L} + \frac{r\tan\delta_b}{L}\right] dx \, , \tag{13}$$

and the axial force by,

$$C_A = \frac{1}{S_o}\int_{x_1}^{x_2}\left[\frac{d(SC_A)}{dx}\right] dx, \tag{14}$$

where S_o is the cross-sectional area of the cylindrical portion of the model. The errors in $\frac{d(SC_N)}{dx}$, C_N, C_m and C_A are estimated to be less than 5 per cent of the respective maximum values pertaining to the appropriate test conditions.

6. RESULTS AND DISCUSSION

6.1 Velocity Profiles

Figure 3 shows typical velocity profiles measured on the models together with a theoretical flat plate profile calculated according to the theory of Chapman and Rubesin (5). A transverse curvature effect is evident in the velocity profile on the 0·16 in diameter model for which the boundary layer is significantly thinner than the theoretical layer. This result is in accord

with the general conclusion of Probstein and Elliott (6) that the term due to transverse curvature in the momentum and energy equations behaves like an external favourable pressure gradient, leading to a thinner boundary layer and an increased slope of the velocity profile at the wall. The velocity profile on the 4·0 in diameter model, which was measured without interference to the flow using the schlieren method, shows good agreement with the theoretical result in the region of the boundary layer near the wall, but a significant thickening of the boundary layer is evident in the outer region. Bradfield et al (7) have shown that a thickening of the boundary layer results from the momentum defect which occurs in the flow over an aerodynamically blunt leading edge*.

6.2 Description of Flow

Figure 4 shows the flow over the 0·16 in diameter model at the lowest Reynolds number $R_L = 0{\cdot}8 \times 10^6$, where boundary layer transition probably commenced in the region of reattachment. At a Reynolds number $R_L = 1{\cdot}2 \times 10^6$, a small degree of laminar separation remained on the model, although the separated layer at the corner was turbulent or nearly so. At higher Reynolds numbers, transition to a turbulent boundary layer occurred naturally upstream of the cylinder-flare junction. The boundary layer on the 4·0 in diameter model remained laminar upstream of the flare at the maximum value of Reynolds number, namely $R_L = 2{\cdot}0 \times 10^6$, used with this model. This result differs from that observed with the 0·16 in diameter model for which transition occurred upstream of the cylinder-flare junction at Reynolds numbers slightly in excess of $1{\cdot}2 \times 10^6$. It is reasonable to assume that the change in transition behaviour results from the difference in the velocity profiles on the models, but it is not clear whether either transverse curvature or leading edge bluntness or the combination of these two effects is the underlying factor in determining the transition behaviour. To provide the necessary turbulent interaction information on the 4·0 in diameter model a boundary layer trip was used, as mentioned earlier, at a Reynolds number $R_L = 2{\cdot}0 \times 10^6$.

6.3 Pressure Distributions

Pressure distributions on the models at zero incidence are shown in figure 5 for a range of Reynolds numbers. Inviscid pressure distributions calculated according to the method of Syvertson and Dennis (1) are included in the figure. The pressure distributions observed at the lower Reynolds numbers are characteristic of laminar separations, in which the interaction region extends over a considerable distance. At the highest Reynolds numbers, the pressure distributions are typical of a turbulent boundary layer at the cylinder-flare junction; the pressure rise is very rapid and the extent of the interaction region is small. It is evident that, except in the region very close to the corner, the inviscid pressure distributions agree reasonably well with the results obtained with turbulent boundary layers. Where a moderate degree of laminar flow separation occurred, the inviscid pressure distributions differ markedly from the experimental results for considerable distances upstream and downstream of the cylinder-flare junction.

Pressure distributions on the 0·16 in diameter model at an incidence of 1° are shown in figure 6 for two Reynolds numbers, $R_L = 0{\cdot}8 \times 10^6$ and $R_L = 2{\cdot}4 \times 10^6$, corresponding to laminar separated flow and turbulent attached flow respectively. The pressure distributions for the laminar separated flow show a greatly increased length of interaction region on the leeward side ($\varphi = 180^\circ$) of the model. The pressure distributions on the windward side ($\varphi = 0^\circ$) and at $\varphi = 90^\circ$ do not differ greatly from the zero incidence pressure distributions. Therefore, a large pressure differential exists on the flare for a considerable region downstream of the cylinder-flare junction, thus giving rise to a large loading on the flare in this region. At the higher Reynolds number, the length of the interaction region is small, and the pressure differential on the flare remains sensibly constant downstream of the junction.

6.4 Normal Force Distributions

Normal force distributions measured on the models at incidence angles of 1° and 4° are shown in figures 7 and 8. Theoretical, inviscid-flow normal force distributions calculated according to the method of Syvertson and Dennis (1) are included for comparison with experiment. At the low Reynolds numbers for which extensive flow separation occurred, the distributions on the 0·16 in diameter model differ significantly from the inviscid distributions at the smaller angle of incidence, but at an incidence of 4°, theory and experiment are in good agreement throughout the Reynolds number range. At 4° incidence, schlieren photographs showed a negligible extent of separation on the model, even at the lowest Reynolds number of the tests, and the good agreement of theory and experiment supports the validity of the theoretical analysis. At a Reynolds number $R_L = 2{\cdot}4 \times 10^6$, for which the boundary layer was turbulent at the cylinder-flare junction, theory and experiment are in good agreement at an angle of incidence of 1°.

* The leading edge radius of the 4·0 in diameter model was 0·0023 in (0·06 mm)

Detailed differences between theoretical and experimental normal force distributions are apparent in the results for the 4·0 in diameter model shown in figure 8. The theoretical distributions agree reasonably well with experiment for distances downstream of the cylinder-flare junction in excess of about 0·5 diameters. Comparison of the experimental results for laminar separation ($R_L = 1{\cdot}2 \times 10^6$) with results for turbulent separation ($R_L = 2{\cdot}0 \times 10^6$t) shows that the loading on the cylindrical portion of the model as well as the loading on the flare is modified by the separation. Downstream of the junction, the pressure rise is generally more abrupt on the windward side of the model leading to a pressure differential which results in a loading in excess of that predicted by theory. This effect is responsible for the difference between the theoretical normal force distribution and that measured for the turbulent boundary layer.

6.5 Total Force and Moment Coefficients

Total force and moment coefficients acting on the flares of the models are shown in figures 9 and 10. The theoretical Syvertson and Dennis (1) results are included in all the figures for comparison purposes. The experimental force and moment coefficients were obtained from equations (12), (13) and (14), where the integrations were made from the cylinder-flare junction over an axial length of 8·7 diameters for the 0·16 in diameter model and 0·75 diameters for the 4·0 in diameter model. At a Reynolds number $R_L = 2{\cdot}4 \times 10^6$, for which a turbulent boundary layer occurred on the 0·16 in diameter model, theory and experiment are in good agreement. At the lowest Reynolds number $R_L = 0{\cdot}8 \times 10^6$, for which extensive laminar separation occurred, significant differences between theory and experiment are evident at small angles of incidence. At zero incidence the axial force is reduced by 22 per cent and the normal force derivative $dC_N/d\alpha$ is increased by a factor of about 5. On a typical flight configuration the greatly increased lift effectiveness of the flare would produce a significant rearward shift of the centre-of-pressure position, thus giving increased static stability. Computations of axial and normal force coefficients were made for a $5{\cdot}4^\circ$ semi-angle conical fairing, which represented the laminar separated flow region. The axial force coefficient calculated in this way is included in figure 9, and shows good agreement with experiment. However, the normal force coefficient calculated with the fairing was in fact slightly less than the normal force coefficient calculated without the fairing.

At small angles of incidence the theoretical and experimental results for the 4·0 in diameter model are in good agreement, but a significant non-linearity is evident in the experimental results at incidence angles in excess of about 2°. The non-linearities are presumably due to the effects of cross-flow, and the linear theory of Syvertson and Dennis, which is valid near zero incidence only, takes no account of these effects. In spite of detailed differences in pressure distributions and normal force distributions due to Reynolds number, the overall force and moment coefficients show only a small Reynolds number dependence. Thus it appears that on a body on which the boundary layer is thin compared to the body radius, and the extent of separation is not great relative to the body diameter, the aerodynamic characteristics are predicted reasonably well at small incidence angles by the inviscid theory of Syvertson and Dennis.

7. CONCLUSIONS

In the absence of separation, the inviscid theory of Syvertson and Dennis gave a good representation of the pressure distribution, loading distribution and the total forces and pitching moment acting on each cylinder-flare model at small angles of incidence. Where a moderate degree of flow separation occurred, the theory underestimated the normal force and overestimated the axial force. Flare lift was increased by flow separation, and a useful gain in static stability was therefore obtained near zero incidence.

8. REFERENCES

1. Syvertson, C.A. and Dennis, D.H.: A Second-Order Shock-Expansion Method Applicable to Bodies of Revolution Near Zero Lift. NACA Report 1328, 1957.
2. Horton, H.P.: The Calculation of Adiabatic Laminar Boundary Layer Shock Wave Interactions in Axisymmetric Flow: Part I - Hollow Cylinder-Flare Bodies with Zero Spin. VKI Technical Note 63, May 1970.
3. Jones, D.J.: Tables of Inviscid Supersonic Flow About Circular Cones at Incidence $\gamma = 1{\cdot}4$, Parts I and II. Agardograph 137, November 1969.
4. Ames Research Staff: Equations, Tables and Charts for Compressible Flow. NACA Report 1135, 1953.
5. Chapman, D.R. and Rubesin, M.W.: Temperature and Velocity Profiles in the Compressible Laminar Boundary Layer with Arbitrary Distribution of Surface Temperature. Jnl. Aero. Sci., Vol. 16, No. 9, September 1949.
6. Probstein, R.F. and Elliott, D.: The Transverse Curvature Effect in Compressible Axially Symmetric Boundary-Layer Flow. Jnl. Aero. Sci., Vol. 23, No.3, March 1956.
7. Bradfield, W.S., DeCoursin, D.G. and Blumer, C.B.: The Effect of Leading-Edge Bluntness on a Laminar Supersonic Boundary Layer. Jnl. Aero. Sci., Vol.21, No.6, June 1954.

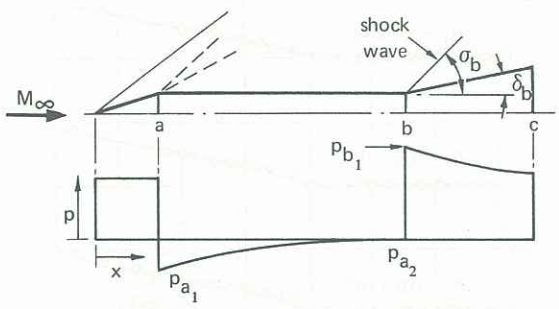

Figure 1. Application of Syvertson and Dennis method

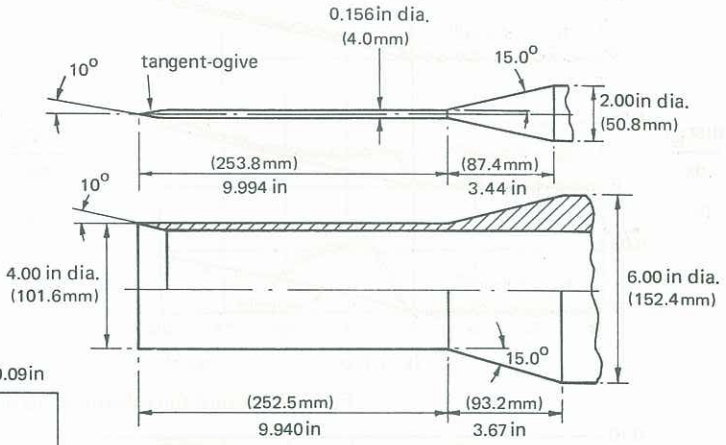

Figure 2. Details of models

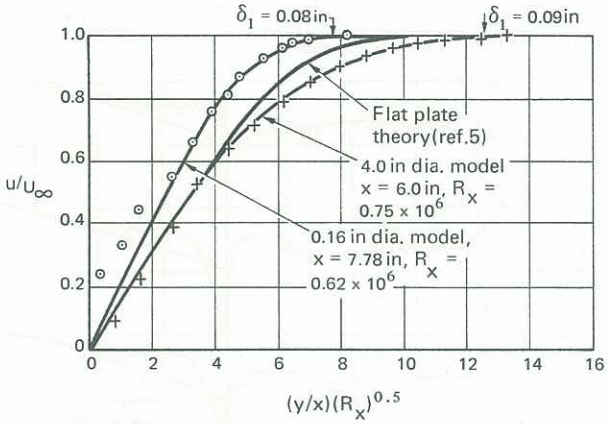

Figure 3. Undisturbed velocity profiles, $\alpha = 0^o$

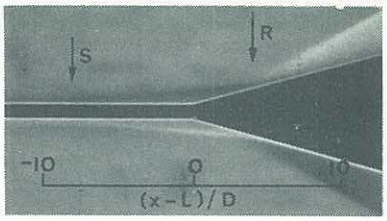

Figure 4. Flow over 0.16in dia. model, $\alpha = 0^o$, $R_L = 0.8 \times 10^6$

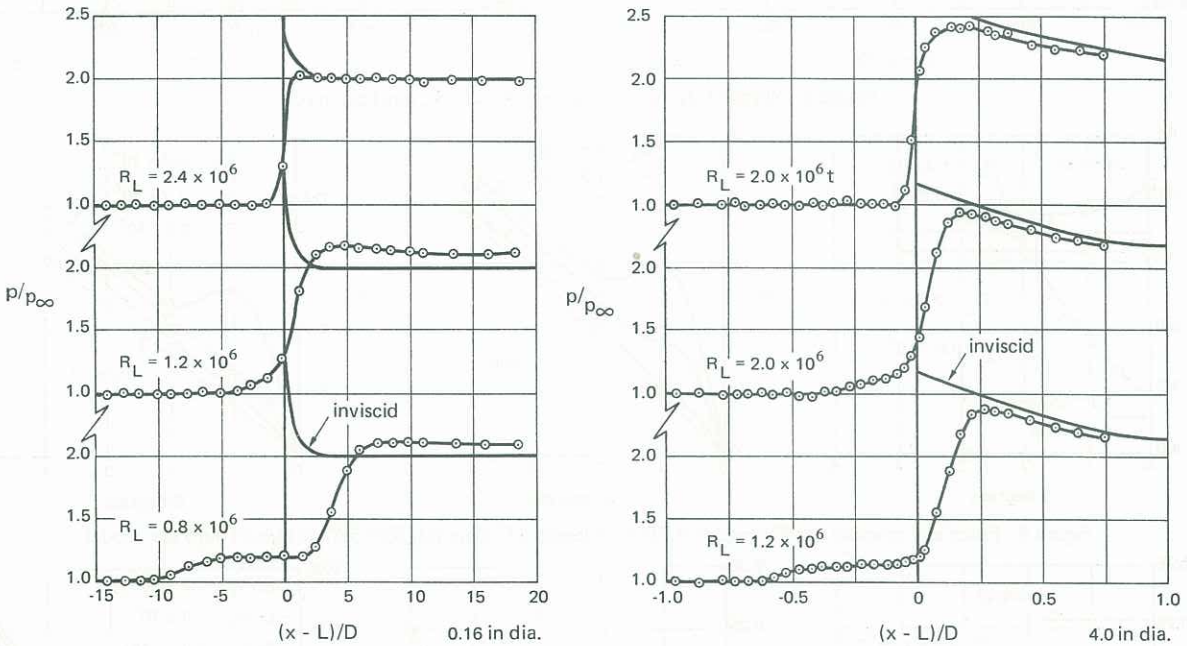

Figure 5. Pressure distributions on models, $\alpha = 0^o$

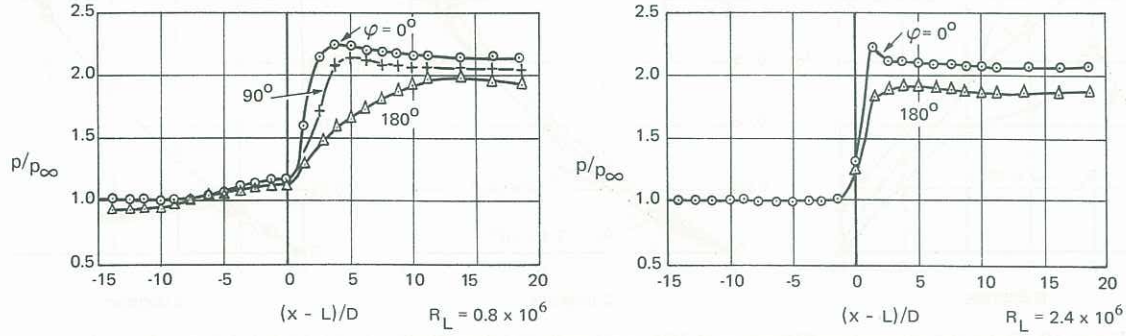

Figure 6. Pressure distributions on 0.16in (4mm) dia. model, $\alpha = 1^o$

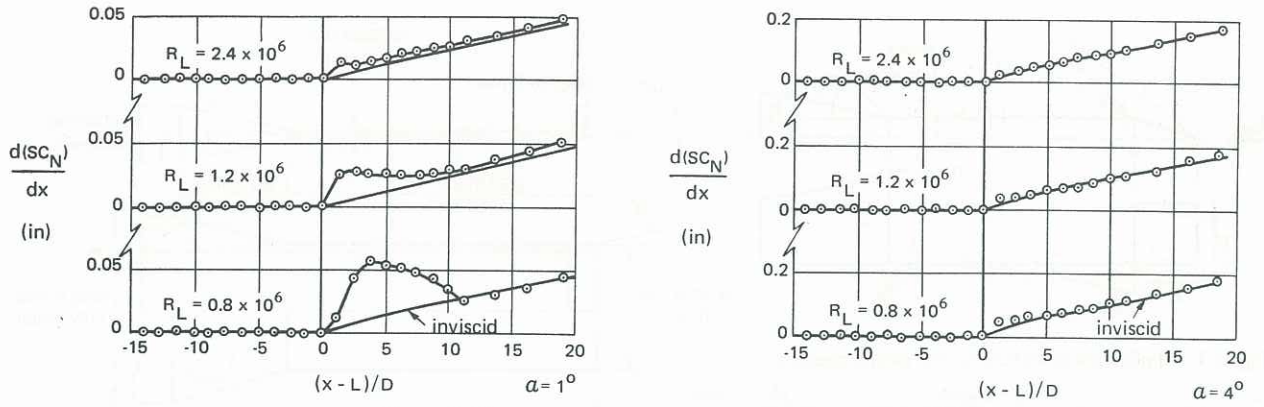

Figure 7. Normal force distributions on 0.16in (4mm) dia. model

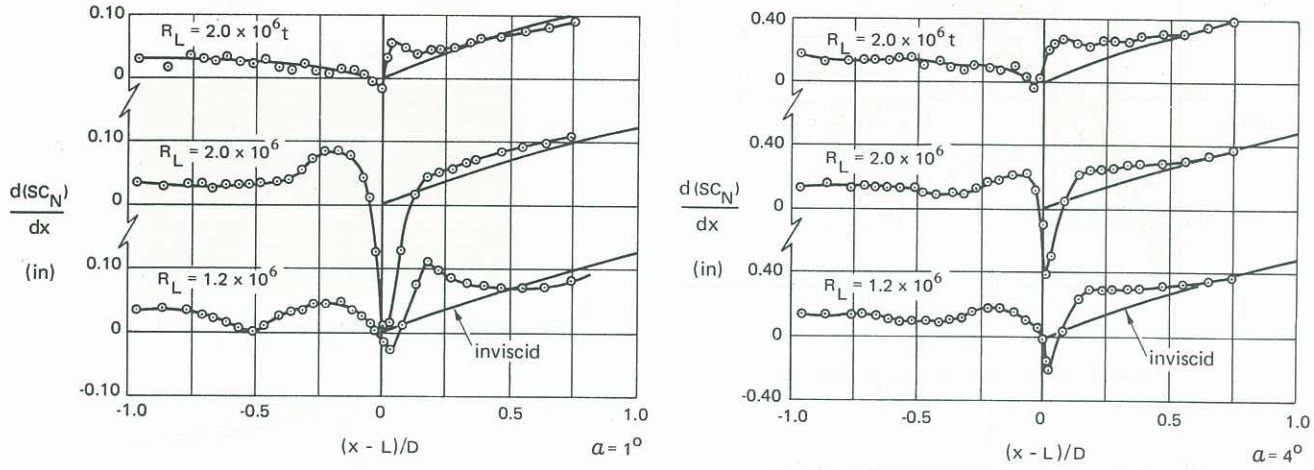

Figure 8. Normal force distributions on 4.0in (102mm) dia. model

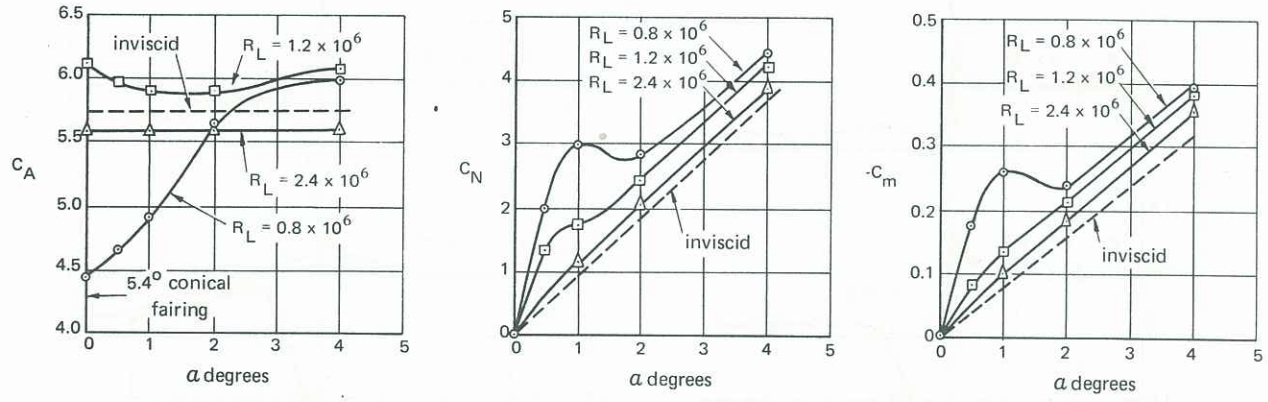

Figure 9. Force and moment coefficients on 8.7D axial length 15° flare ($D_b/D = 5.6$), 0.16in (4mm) dia. model

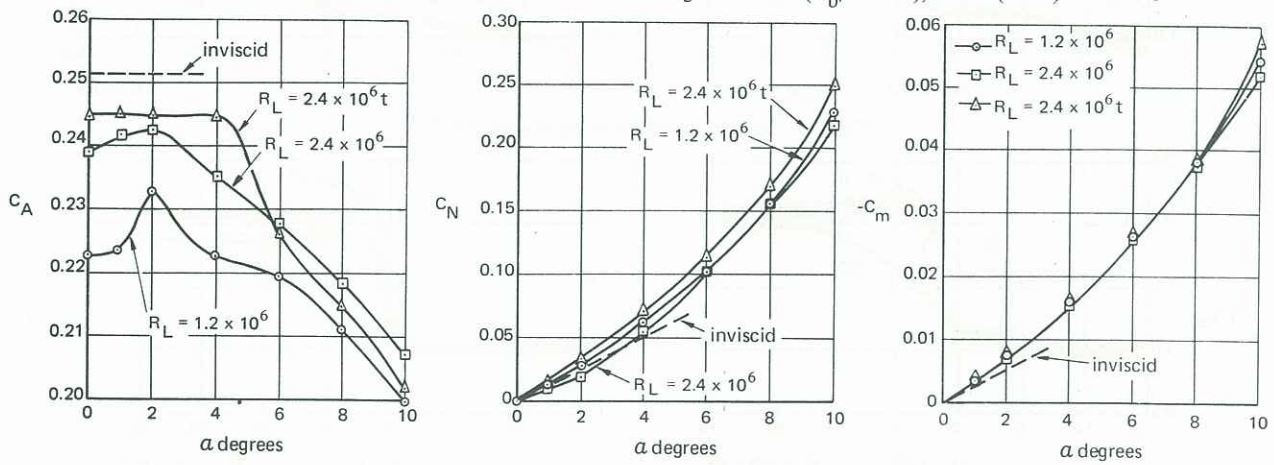

Figure 10. Force and moment coefficients on 0.75D axial length 15° flare ($D_b/D = 1.41$), 4.0in (102mm) dia. model